VORTEX STRUCTURES IN THE SEPARATED FLOW ON AN INCLINED FLAT PLATE UNDER ELECTROMAGNETIC FORCING: INFLUENCES OF EXCITATION WAVE FORM, FREQUENCY, AND AMPLITUDE

Tom Weier, Christian Cierpka, Gunter Gerbeth
Magneto–Hydrodynamics Division,
Forschungszentrum Dresden–Rossendorf
Bautzner Landstr. 128, D–01328 Dresden, Germany
{t.weier,c.cierpka,g.gerbeth}@fzd.de

ABSTRACT

Wall parallel Lorentz forces have been used to excite the separated flow on the suction side of inclined symmetric hydrofoils. Resulting lift enhancements resemble those known from alternative active flow control methods. The controlled flow is characterized by a small number of relatively large vortices, which are related to the control mechanism. Consequently, time resolved flow fields have been analyzed by proper orthogonal decomposition and continuous wavelet transform to extract dominant features. Both evaluation methods highlight significant influences of excitation frequency, wave form, and amplitude.

INTRODUCTION

Flow separation and its control is a persistent topic of fluid dynamic research with large technological importance. A recent and comprehensive review is that of Gad–el–Hak (2000). Since the early 1990s, separation control by periodic addition of momentum, now commonly termed "active flow control", has been a subject of intense research. Its main advantage compared to steady actuation is that a control goal, e.g. a specific lift increase, can typically be attained by orders of magnitude smaller momentum input (Greenblatt and Wygnanski, 2000). The most significant actuation parameters are the time averaged momentum input c'_μ and the normalized excitation frequency F^+.

Actuator properties and excitation parameters are obviously the key issues for application as well as research in the area of active flow control. Electromagnetic – i.e. Lorentz – forces offer attractive features in this respect: momentum is generated directly in the flow without associated mass flux, the frequency response of the actuation and the choice of the excitation wave form are practically unlimited, no moving parts are involved. To date, owing to the relatively weak permanent magnetic fields readily available ($B = O(1)\,\mathrm{T}$), these advantages are accompanied by a low energetical efficiency in low conducting fluids which prevents industrial application. However, Lorentz force actuators are a valuable tool in basic research. For detailed information and an historical overview, we refer to Weier et al. (2007).

Fig. 1 displays force balance data acquired on a NACA 0015 under electromagnetic flow control. At a Reynolds number of $Re = 0.8 \times 10^5$ the flow is excited with a sinusoidal current at a normalized frequency of $F^+ = 0.5$, which is in the optimal range of $F^+ = O(1)$. Further details are described in Weier and Gerbeth (2004). The time averaged lift coefficient (left) shows the expected monotonic increase with the rms momentum coefficient c'_μ. Phase averages of the lift coefficient depend strongly on the excitation, as has been observed before in, e.g., the numerical work of Wu et al. (1998). This significant unsteadiness is a clear hint to the presence of vortex shedding in the controlled flow. Since the control mechanism is believed to be based on an intensified momentum transfer between free stream and separated flow caused by the vortices, it seems desirable to observe these vortices directly.

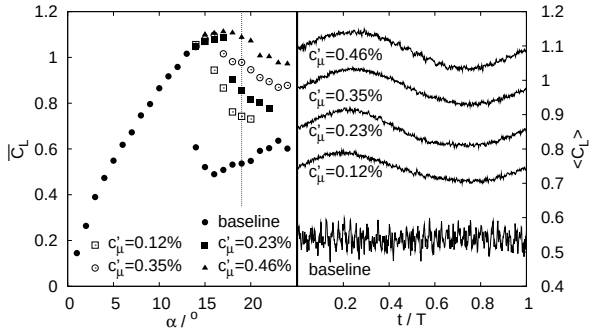

Figure 1: Mean lift *versus* angle of attack for a NACA 0015 at $Re = 0.8 \times 10^5$, $F = 0.5$ and different momentum coefficients (left). Phase averaged lift at $\alpha = 19°$ for otherwise identical conditions (right, baseline is not averaged).

The present study is also partly motivated by the significant influence of the excitation wave form on the attainable lift gain found previously by Weier and Gerbeth (2004). Under otherwise identical conditions (Re, angle of attack α, F^+, c'_μ), lift coefficients of a NACA 0015 under excitation varied by 70% depending on the excitation wave form. Similar effects have been observed by Margalit et al. (2002) using piezoelectric actuators driven by an amplitude modulated signal. Up to now, an explanation for the observed large differences in lift is, to the knowledge of the authors, not available. However, it is known that different excitation parameters cause different vortex structures in the separated flow. It is conjecturable that the differences in lift observed, using e.g. different excitation wave forms, might be connected to variations of these vortex structures. In the following, time resolved particle image velocimetry (TR–PIV) measurements and data processing in order to educe characteristic vortex structures are described.

EXPERIMENTAL SETUP AND PARAMETERS

To gain first insight into the instationary and complex flow phenomena under excitation, the suction side flow field of an inclined flat plate was investigated. The plate, sketched in Fig. 2, has been equipped with a stripwise arrangement of flush mounted electrodes and permanent magnets. Such

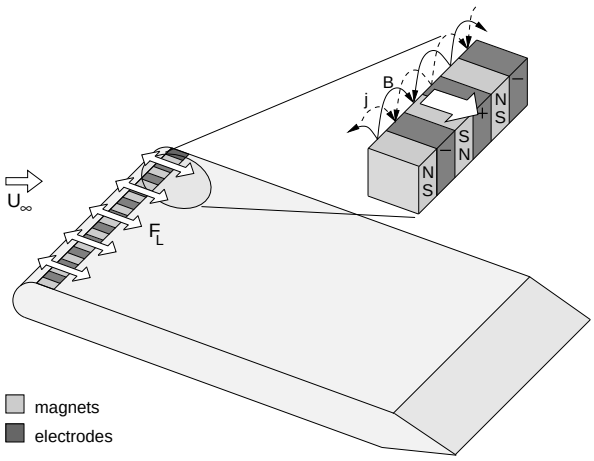

Figure 2: Sketch of the inclined flat plate with the Lorentz force actuator at the leading edge.

a combination of electrodes and magnets produces a wall parallel Lorentz force F_L in streamwise direction. In the case of weakly electrically conducting fluids considered here, the Lorentz force is simply the vector product of the applied current density $\boldsymbol{j}$ and the applied magnetic induction $\boldsymbol{B}$: $\boldsymbol{F} = \boldsymbol{j} \times \boldsymbol{B}$. An alternating current generates a Lorentz force oscillating in streamwise direction with the frequency f_e of the applied current. The normalized excitation frequency

$$F^+ = \frac{f_e c}{U_\infty} \tag{1}$$

is defined with the chord length c and the free stream velocity U_∞. The momentum input is characterized by the effective momentum coefficient

$$c'_\mu = \frac{1}{2} \cdot \frac{aB_0}{\rho U^2} \cdot \frac{l}{c} \cdot \sqrt{\frac{1}{T} \int_0^T j(t)^2 \mathrm{d}t} \tag{2}$$

where a denotes the width of an electrode, l their length, $j(t)$ the time dependent current density, T the period of oscillation, B_0 the magnetic induction at the surface of the permanent magnets and ρ the fluid density.

The PIV measurements reported in the following were performed in an electrolyte channel filled with a dilute sodium hydroxide solution. The test section of this free surface channel is 1 m long and has a $0.2 \times 0.2\,\mathrm{m}^2$ cross section. A flow speed of 0.08 m/s, resulting in a chord length Reynolds number of $Re = 1.04 \times 10^4$ has been used throughout the measurements. For further details on the channel, we refer to Weier (2006). A 10 mm thick plate made from PVC with a circular leading edge, a span of 140 mm and a chord length of 130 mm served as hydrofoil. A mean magnetic induction of $B_0 = 0.35\,\mathrm{T}$ could be measured at the surface of the NdFeB–magnets. To reduce end effects, the plate has been mounted between rectangular plates with rounded edges made from perspex. These end plates reached from the bottom of the test section to the free surface in vertical and from 30 mm in front of the leading edge to 30 mm behind the trailing edge in horizontal direction. For the electrical field generation a high power amplifier FM 1295 from FM Elektronik Berlin has been used to feed the electrodes. It was driven by a frequency generator Agilent 33220A allowing for different frequencies, wave forms and amplitudes of the Lorentz force.

The PIV setup consists of a Spectra Physics continuous wave Ar^+–Laser type 2020–5 as light source. For the image recording a Photron Fastcam 1024PCI 100K operated at 60 Hz frame rate was used. The light sheet with a thickness of $\Delta z \approx 1$ mm was formed by two cylindrical lenses. It entered through the bottom of the test section, extended in the x–y–plane and was positioned at mid–span. Since the laser operated in continuous mode, the camera shutter was used to set the image exposure time to 2 ms. For each configuration, a total of 6400 single images of 1024×512 pixel have been recorded synchronized to the excitation signal. Polyamide particles (Vestosint) of 25 μm mean diameter were chosen to seed the flow. In the plane of the light sheet, x and y velocity components (u,v) have been calculated from the images using PIVview–2C 2.4 from PivTec. Each image was correlated with its successor using multigrid interrogation with a final window size of 16×16 pixel^2 and 50% overlap, image deformation and sub pixel shifting was applied as well.

POSTPROCESSING

Continuous Wavelet Transform

Obviously, since the flow is inherently instationary and the mechanisms involved are quite complex, the averaged velocity fields hide important flow features. To overcome these limitations to a certain extend, phase averaging based on the dominant frequency of the process, F^+, can be applied Cierpka et al. (2007). However, in case of arbitrary excitation wave forms, peaks of comparable height may occur in the power spectra for several frequencies connected to the Fourier coefficients of the excitation signal. In such a case, the choice of a proper dominant frequency becomes complicated. Nevertheless, it is a necessary precondition for data interpretation to condense the vast amount of information provided by the TR–PIV measurements. To extract coherent structures from the time resolved velocity fields several methods have been proposed, see e.g. Bonnet et al. (1998). In the present study the continuous wavelet transform (CWT) as well as proper orthogonal decomposition (POD) was chosen to analyse the TR–PIV data.

An extensive review of wavelet transforms and their application to fluid dynamics can be found in Farge (1992). For the CWT, we followed the approach proposed by Schram et al. (2002). A two dimensional Marr or Mexican hat wavelet has been used to analyse the time resolved vorticity fields. Different vortex characteristics such as vortex size and circulation, trajectories, and mean convection velocities can be determined. In the following, some practical aspects of the implementation are given. The procedure follows closely that introduced by Schram (2002), although the vortex detection here is based on the vorticity field

$$\omega_z = \frac{\partial v}{\partial x} - \frac{\partial u}{\partial y} \tag{3}$$

instead of the enstrophy field. The vorticity field is a well suited basis to detect vortices, because it is Galilean invariant and vortices are regions of high vorticity. Since a prominent shear layer is present in the observed flow fields as well, the λ_2-criteria from Jeong and Hussain (1995) was used to identify coherent structures and to separate them from the shear layer. In regions, where no vortices would be expected according to the λ_2-criteria, i.e. for $\lambda_2 \geq 0$, the vorticity field has been set to zero. The wavelet analysis was then applied to this modified vorticity field. In contrast to the Fourier analysis, the wavelet analysis is selective in space and scale and therefore an appropriate tool for the investigation of coherent structures. The wavelet transform of a

signal is given by the convolution of the signal $f(\boldsymbol{x})$ and the wavelet family $\Psi_{l\boldsymbol{x}'}$

$$\langle \Psi_{l\boldsymbol{x}'} | f \rangle = \int_{R^n} f(\boldsymbol{x}) \Psi^*_{l\boldsymbol{x}'}(\boldsymbol{x}) d^n \boldsymbol{x} \tag{4}$$

where Ψ^* denotes the complex conjugate of Ψ, $\boldsymbol{x}'$ the position and l the scale of the wavelet, respectively. The two dimensional Marr wavelet is defined in polar coordinates as

$$\Psi(r,l) = \frac{1}{l}\left(2 - \frac{r^2}{l^2}\right) \exp\left(-\frac{r^2}{2l^2}\right) \tag{5}$$

The choice of this mother wavelet is justified by assuming a Gaussian distribution of vorticity in the coherent structures.

In order to relate the wavelets to the coherent structures, a model vortex had to be chosen. Following Schram (2002), the Lamb–Oseen vortex is used here. This vortex, constituting an exact solution of the Navier–Stokes equations, is defined as follows

$$u_\phi(r) = \frac{\gamma}{2\pi r}\left[1 - \exp\left(-\frac{r^2}{2\sigma^2}\right)\right] \tag{6}$$

$$\omega(r) = \frac{\gamma}{2\pi\sigma^2} \exp\left(-\frac{r^2}{2\sigma^2}\right) \tag{7}$$

u_ϕ denotes the tangential velocity, γ the circulation and σ the size of the vortex, respectively. The size of the vortex core D_c is usually defined by the maximum of the tangential velocity and thus $D_c = 2r_c = 3.17\sigma$ for the Lamb–Oseen vortex. Its wavelet coefficient is defined as

$$\langle \Psi_l | \omega \rangle = \int_0^{2\pi}\int_0^{\infty} \frac{\gamma}{2\pi\sigma^2} \exp\left(\frac{-r^2}{2\sigma^2}\right) \cdot \frac{1}{l}\left(2 - \frac{r^2}{l^2}\right) \exp\left(-\frac{r^2}{2l^2}\right) r \mathrm{d}r \, \mathrm{d}\phi \tag{8}$$

Differentiating (8) with respect to the scale results in

$$\frac{\partial \langle \Psi_l | \omega \rangle}{\partial l} = -\frac{2\gamma l^2 \left(l^2 - 3\sigma^2\right)}{\left(l^2 + \sigma^2\right)^3} \tag{9}$$

For the Lamb–Oseen vortex size σ and the scale l that maximizes the wavelet transform of its vorticity field therefore $l/\sigma = \sqrt{3}$ holds. Using this relation it is possible to associate a certain vortex core diameter with the maximum wavelet coefficient. In order to have the best possible choice for the wavelet scales, the algorithm calculates the size of possible structures in advance and adjusts the scales for the test wavelets. Using this procedure makes the scale detection more precise and saves computational time.

A second criteria determines the likeness of the detected structure to a vortex. The absolute value of the wavelet coefficient $\langle \Psi_l | \omega \rangle$ depends on the size of a vortex and its strength. From Eq. (7) the circulation γ at the vortex center writes

$$\gamma_0 = 2\pi\sigma^2\omega_0 \qquad \text{for } (r = 0)\,. \tag{10}$$

Using the relation $l/\sigma = \sqrt{3}$ and γ_0 in Eq. (8), the maximum wavelet coefficient depends only on the wavelet scale l and center vorticity ω_0:

$$\langle \Psi_l | \omega \rangle_{th} = \frac{3}{4}\pi\omega_0 \, l \tag{11}$$

Since the vorticity at the center is known, a likeness β giving the ratio of the actually determined wavelet coefficient to the theoretical one expected for a Lamb–Oseen vortex, can be calculated.

$$\beta = \frac{\langle \Psi_l | \omega \rangle}{\langle \Psi_l | \omega \rangle_{\mathrm{th}}} \tag{12}$$

Only structures with a likeness of more than $\beta = 80\%$ have been assumed to be vortices.

Proper Orthogonal decomposition

Proper orthogonal decomposition (POD) is nowadays almost a standard technique to analyse flow fields. An overview with applications to fluid mechanics can be found, e.g., in Cordier and Bergmann (2003). The basic idea is to find an approximation of the function

$$f(\boldsymbol{x},t) \approx \sum_{k=1}^{K} a_k(t)\, \Phi_k(\boldsymbol{x}) \tag{13}$$

which tends to be exact for $K = \infty$. The (POD) basis functions $\Phi_k(\boldsymbol{x})$ are chosen to be orthonormal and as good as possible for each K in a least square sense (Cordier and Bergmann, 2003). Considering $f(\boldsymbol{x},t)$ as a flow variable, measured at N_t instants of time, Eq. (13) translates into finding basis functions that fulfill:

$$\min \sum_{i=1}^{N_t} \left\| f(\boldsymbol{x},t_i) - \sum_{k=1}^{K} \left(f(\boldsymbol{x},t_i), \Phi_k(\boldsymbol{x})\right) \Phi_k(\boldsymbol{x}) \right\|_2^2 \tag{14}$$

where $\|.\|_2$ is the L_2 norm and $(.,.)$ the inner product of two quantities. When the velocity is used as input data, the POD modes are optimal in terms of energy, vorticity data result in enstrophy optimal modes instead. In the present paper, following Kostas et al. (2005), vorticity fields ω_z (Eq. 3) have been decomposed. By adequately ordering the measurements into a matrix A the problem can be solved by standard singular value decomposition (SVD) routines.

$$A = U\sigma V^T \tag{15}$$

$A(N_t, N_{\boldsymbol{x}})$ denotes the matrix of the measurements. σ is the diagonal matrix of singular values in decreasing order $(\sigma_1 \geq \sigma_2 \ldots \sigma_{r-1} \geq \sigma_r \geq 0)$ with $r = \min(N_t, N_{x,y})$. The first r columns of $U = (u_1, u_2, \ldots, u_{N_t})$ are the left singular vectors and the first r columns of $V = (v_1, v_2, \ldots, v_{N_{\boldsymbol{x}}})$ are the right singular vectors of A and correspond to the POD modes Φ_k.

The data produced by the TR–PIV are of the order of $N_t = 6400$ realizations in time with $N_{\boldsymbol{x}} \approx 8000$ vectors each for one parameter configuration. Solving this by SVD results in a huge numerical problem, requiring a large amount of computational memory and time. To decrease this effort, we use the snapshot method proposed by Sirovich (1987). By premultiplying A with its transpose one ends up with the eigenvalue problem

$$A^T A\nu = \lambda\nu \tag{16}$$

where λ are the eigenvalues and ν the eigenvectors of $A^T A$. The singular values are $\sigma = \sqrt{\lambda}$ and the POD modes can be calculated using

$$\Phi_k = \frac{1}{\sqrt{\lambda_k}} A\nu_k. \tag{17}$$

The problem size is thereby reduced significantly. Eigenvalue routines provided by the GNU scientific library (GSL) have been used.

Since the separated flow over the inclined plate is relatively complex, both algorithms, the CWT and POD, have been tested and verified to work well for the flow around a circular cylinder.

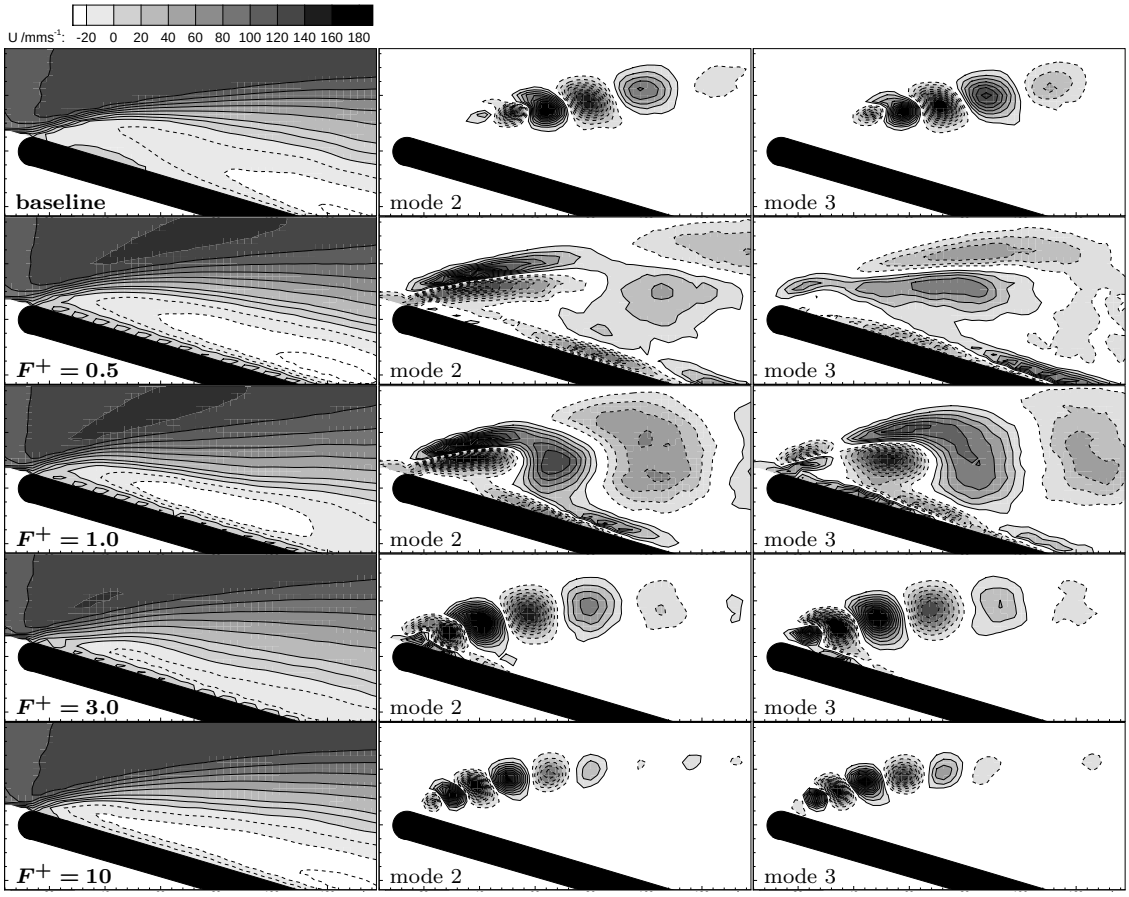

Figure 3: Mean velocity (left column) and second and third POD mode for baseline flow (top) and sinusoidal excitation with $c'_\mu = 2.6\%$ and different F^+ at $\alpha = 17°$.

RESULTS

Excitation Frequency

In Figure 3 the distribution of the averaged streamwise velocity u is shown on the left. Negative values, i.e. backflow, are marked by dashed lines and can be used to indicate the size of the separation region. In the baseline flow (top) a huge region of decelerated flow is visible above the plate extending beyond the trailing edge in streamwise direction. Using sinusoidal excitation with $c'_\mu = 2.6\%$ and different frequencies the size of this region is decreased. A forcing with $F^+ = 1$ results in reattachment of the mean flow. For $F^+ = 3$ there seems to be almost no separation. A further increase of the excitation frequency results again in a growing separation region. At $F^+ = 10$, backflow occurs even closer to the leading edge as without forcing.

The pairwise occurring POD modes 2 and 3 of ω are plotted in the middle and on the right of Fig. 3. Dashed contour lines identify negative values. Since the total vorticity was decomposed, the first mode belongs to the mean flow and is not of interest regarding the periodic phenomena (Siegel et al., 2007).

For the baseline flow, the natural vortex shedding from the shear layer results in a row of structures located in the region of high mean shear. Since the shear layer starts to roll up after a certain distance from the leading edge only, there are no visible structures directly at the leading edge. In contrast to that, for all cases with excitation, structures in the POD modes can be observed already at the leading edge. Obviously, the actuation leads to an earlier formation of vortices. For lower excitation frequencies, the structures are large and relatively complicated in shape. In the case of $F^+ = 0.5$ the structures are strongly elongated in streamwise direction and situated mainly in the region of strong mean shear. An excitation with $F^+ = 1$ produces structures which are much less elongated and have a larger extension in cross stream direction. They come closer to the plates surface, indicating a stronger momentum exchange between the separated region and the free stream. For the excitation with $F^+ = 3$ compact structures form directly at the leading edge. Their size is much smaller than for $F^+ = 1$, but larger than in the baseline case. An intensive momentum transfer between free stream and wall near fluid in the region near the leading edge may be deduced, which is supposed to be the reason for the suppression of backflow. With increasing frequency the structures generated by the actuator become smaller. At $F^+ = 10$ the modes look somewhat similar to the baseline case, although their frequency is higher and they appear nearer to the leading edge. In return, they seem to decay faster.

The influence of the excitation frequency is also visible in the mean vortex characteristics extracted by the CWT–algorithm. In the bottom part of Fig. 4 the averaged pathlines of the vortex centers detected by the CWT are shown. For the different frequencies, the vortices start to appear at almost the same point. For the baseline flow, the mean vortex trajectory is further away from the plates surface compared to the forced flow cases. Especially the excitation with $F^+ = 1$ moves the trajectory closer to the surface, allowing for a more intense interaction of the vortices with the separation region.

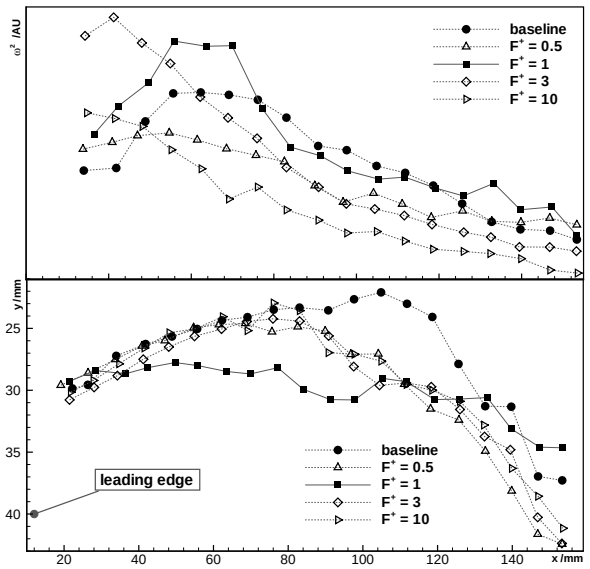

Figure 4: Streamwise distribution of the enstrophy content (top) and averaged pathline (bottom) for baseline flow and sinusoidal excitation with $c'_\mu = 2.6\%$ and different F^+ at $\alpha = 17°$.

However, the forcing with $F^+ = 3$ produces structures with the largest enstrophy content especially close to the leading edge, compared to the other forcing frequencies. This can be seen from Fig. 4, where averages of the vortex enstrophy are shown. The curve for $F^+ = 3$ has a peak near the leading edge due to the production of small but strong vortices. With increasing downstream distance, these structures lose their energy and dissipate soon. Similar effects can bee observed for the forcing with $F^+ = 10$, again the enstrophy in the production region is high, but decays early. For the forcing with frequencies around the natural frequency, the trends of the enstrophy distribution are quite analogue. Weak energy structures are built upstream which gain enstrophy at the point they separate from the shear layer at around $x \approx 60\,\mathrm{mm}$. For the lower frequency the forcing with half of the natural frequency results in a suppression of this energy gain compared to the baseline flow, in the case for $F^+ = 1$ when the natural and excitation frequency are synchronized this gain is very prominent. The slower decay of enstrophy with downstream direction for these excitation frequencies is probably caused by the feeding of the vortices by rich momentum fluid from the outer flow.

Excitation Amplitude

The influence of the excitation amplitude on the separated flow at the 13° inclined plate can be seen in Fig. 5. The region with backflow decreases with increasing momentum coefficient and vanishes completely for $c'_\mu = 2.0\%$. For the baseline flow, the POD modes due to shear layer vortex shedding, are similar to that observed for an inclination angle of 17°, see Fig. 3. Excitation at $F^+ = 1$ leads to larger structures forming closer to the leading edge. For $c'_\mu = 2.0\%$ the structures are located in the direct vicinity of the plate, which indicates that the fluid flow follows the plates contour.

Excitation Wave Form

An example for the influence of the excitation wave form on the separated flow shows Fig. 6. A rectangular signal with a variable duty cycle but a constant rms momentum coefficient of 2.6% and zero mean value, i.e. alternating pulses with positive and negative amplitudes, has been used for the actuation. Despite the constant rms momentum input, the mean flow fields differ from each other particularly in the size of the reversed flow region. Though it can not be suppressed completely at 17° inclination angle, it is smallest for a duty cycle of 0.25. While the POD modes near the leading edge change their shape, the mean flow there is relatively insensitive to the duty cycle. The differences in the mean flow occur near the trailing edge and are probably connected to the lifetime of the structures and their ability to transfer momentum from the mean flow. Presumably, the structures energy increases with the peak momentum input, i.e. with decreasing duty cycle. However, there is obviously an optimum, which might be explained by the capability of the flow to react on the actuation. In addition, if the duty cycle gets too short, natural vortex shedding reappears in the off–phase.

ACKNOWLEDGEMENTS

Financial support from Deutsche Forschungsgemeinschaft (DFG) in frame of the Collaborative Research Centre (SFB) 609 is gratefully acknowledged.

REFERENCES

Bonnet, J. P., Delville, J., Glauser, M. N., Antonia, R. A., Bisset, D. K., Cole, D. R., Fiedler, H. E., Garem, J. H., Hilberg, D., Jeong, J., Kevlahan, N. K. R., Ukeiley, L. S., Vincendeau, E., 1998, "Collaborative testing of eddy structure identification methods in free turbulent shear flows", *Exp. Fluids*, Vol. 25, pp. 197–225.

Cierpka, C., Weier, T., and Gerbeth, G., 2007, "Electromagnetic control of separated flows using periodic excitation with different wave forms", *Notes on Numerical Fluid Mechanics and Multidisciplinary Design*, Vol. 95, R. King, ed., Springer, in press.

Cordier, L., and Bergmann, M., 2003, "Proper orthogonal decomposition, an overview" *VKI LS 2003–03, Postprocessing of Experimental and Numerical Data*, von Karman Institute for Fluid Dynamics, Belgium.

Farge, M., 1992, "Wavelet transforms and their application to turbulence", *Annu. Rev. Fluid Mech.*, Vol. 24, pp. 395–457.

Gad–el–Hak, M., 2000, "Flow control: passive, active, and reactive flow management.", Cambridge University Press, Cambridge.

Greenblatt, D., and Wygnanski, I., 2000, "The control of flow separation by periodic excitation", *Prog. Aerosp. Sci.*, Vol. 36, pp. 487–545.

Jeong, J., and Hussain, F., 1995, "On the identification of a vortex", *J. Fluid Mech.*, Vol. 285, pp. 69–94.

Kostas, J., Soria, J., and Chong, M. S., 2005, "A comparison between snapshot POD analysis of PIV velocity and vorticity data.", *Exp. Fluids*, Vol. 38, pp. 146–160.

Margalit, S., Greenblatt, D., Seifert, A., and Wygnanski, I., 2002, "Active flow control of a delta wing at high incidence using segmented piezoelectric actuators", *AIAA paper 2002–3270*

Schram, C., 2002, "Application of wavelet transform in vortical flows." *VKI LS 2002–04, Postprocessing of Experimental and Numerical Data*, von Karman Institute for Fluid Dynamics, Belgium.

Siegel, S., Cohen, K., Seidel, J., and McLaughlin, T.,

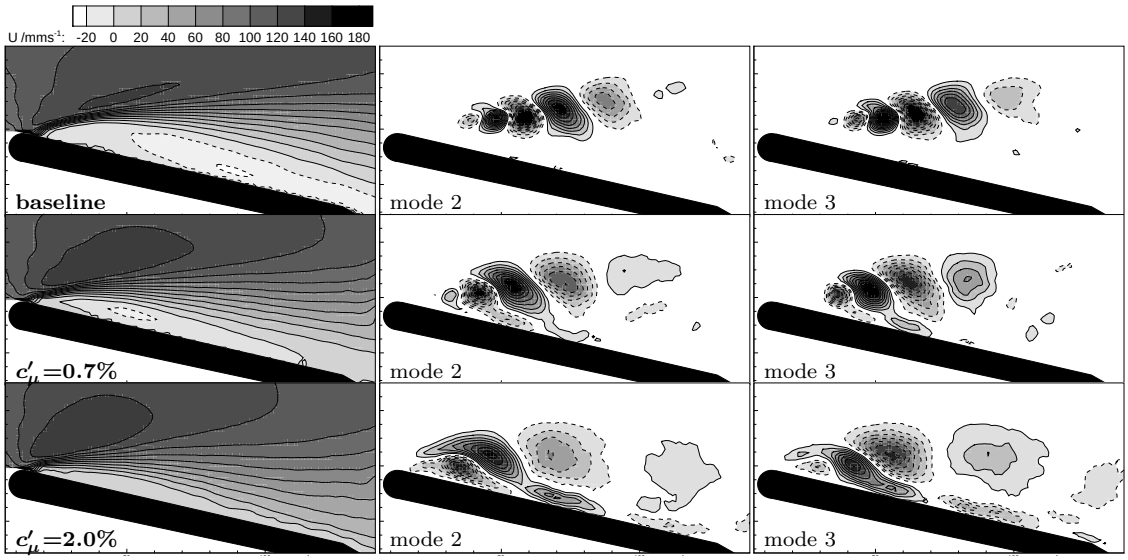

Figure 5: Averaged velocity and second and third POD mode for baseline flow (top) and excitation with a rectangular wave form of 25% duty cycle at $F^+ = 1$, $\alpha = 13°$ and different momentum coefficients.

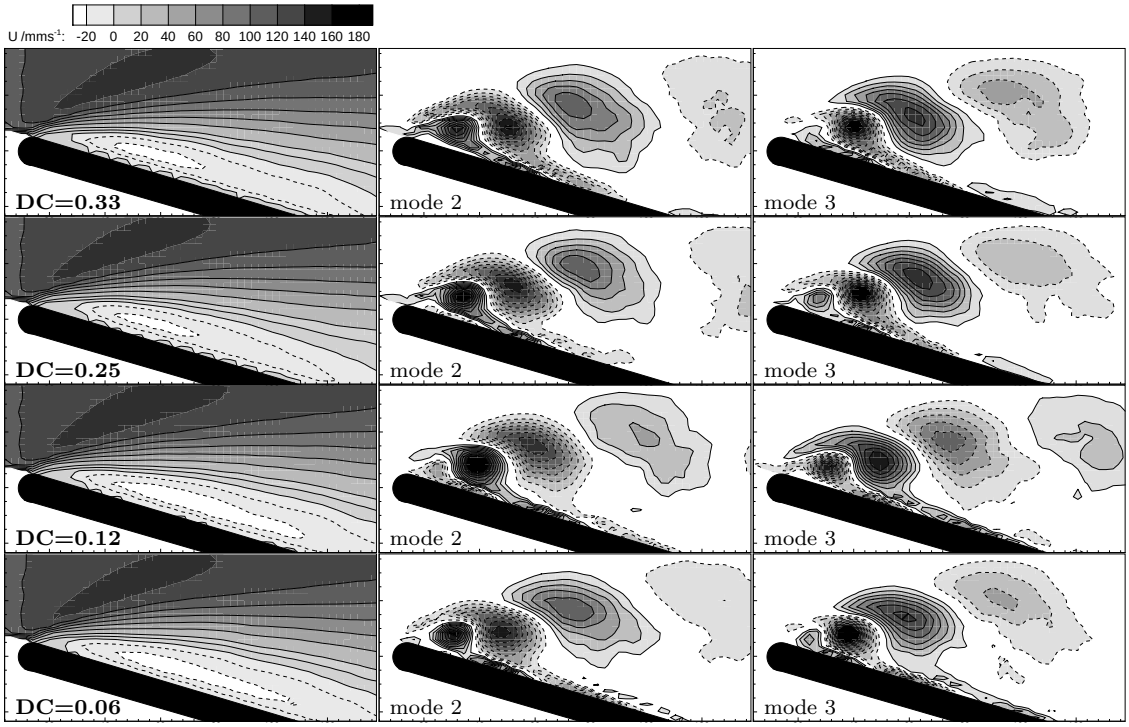

Figure 6: Averaged velocity and second and third POD mode for excitation with a rectangular wave form of different duty cycle at $c'_\mu = 2.6\%$, $\alpha = 17°$and $F^+ = 1$.

2007, "State estimation of transient flow fields using double proper orthogonal decomposition (DPOD)", *Notes on Numerical Fluid Mechanics and Multidisciplinary Design*, Vol. 95, R. King, ed., Springer, in press.

Sirovich, L., 1987, "Turbulence and the dynamics of coherent structures. Part I: Coherent structures", *Quarterly of Applied Mathematics*, Vol. 45, pp. 561–571.

Weier, T., and Gerbeth, G., 2004, "Control of separated flows by time periodic Lorentz forces", *Eur. J. Mech. B/Fluids*, Vol. 23, pp. 835–849.

Weier, T., 2006, "Elektromagnetische Strömungskontrolle mit wandparallelen Lorentzkräften in schwach leitfähigen Fluiden", Ph.D. Thesis, Technical University Dresden, Dresden.

Weier, T., Shatrov, V., and Gerbeth, G., 2007, "Flow control and propulsion in poor conductors". *Magnetohydrodynamics – Historical Evolution and Trends* S. Molokov, R. Moreau, H. K. Moffatt, eds., Springer, pp. 295–312.

Wu, J.–Z., Lu, X.–Y., Denny, A. G., Fan, M., and Wu, J.–M., 1998, "Post–stall flow control on an airfoil by local unsteady forcing", *J. Fluid Mech.*, Vol. 371, pp. 21–58.